

INTERCONNECTION OF SILICON HETEROJUNCTION SOLAR CELLS BY INFRARED SOLDERING – SOLDER JOINT ANALYSIS AND TEMPERATURE STUDY

Angela De Rose^{1,2*}, Torsten Geipel¹, Dirk Eberlein¹, Achim Kraft¹, and Mathias Nowottnick²
¹Fraunhofer Institute for Solar Energy Systems ISE, Heidenhofstr. 2, 79110 Freiburg, Germany
²University of Rostock, IEF/IGS, Albert-Einstein-Str. 2, 18059 Rostock, Germany
*Phone: +49 (0)761 4588 5856, angela.de.rose@ise.fraunhofer.de

ABSTRACT: Interconnection of silicon heterojunction (SHJ) solar cells by soldering is challenging due to the temperature sensitivity of the passivation layers. Within our study, we evaluate solder joints on SHJ solar cells interconnected by infrared (IR) soldering. We screen printed various low-temperature metallization pastes on industrial precursors and interconnected them with Sn60Pb40 coated Cu ribbons on an industrial IR stringer. For our analysis, we used a temperature profile for soldering according to the industrial standard of PERC cells (~240 °C, < 3 s). Adhesion after soldering was characterized by 90° peel tests, yielding improved values of 0.9 N/mm. Microstructural investigations reveal a defined Ag₃Sn layer, indicating a proper metallurgical bond. With electrical characterizations at cell and module level, we show IR soldering to be feasible for the interconnection of SHJ solar cells. We built 3-cell-modules and measure a power degradation below 1.5 % after 200 temperature cycles (-40 °C/+85 °C). A successful interconnection is also shown by a cell-to-module power ratio of 98.8 % for a 60-cell-module achieving 324 W.

Keywords: Interconnection, Heterojunction, Soldering, Modules, Reliability

1 INTRODUCTION

Carrier-selective passivating contacts promise a photoconversion efficiency advantage and are widely recognized as one of the most probable future mass production technologies [1, 2]. Most passivating contacts are realized by a heterojunction structure with an *a*-Si/*c*-Si interface (silicon heterojunction, SHJ). Amorphous silicon layers have been shown in literature to degrade severely when exposed to temperatures above ~220 °C for longer durations [3–5], limiting the possibilities of usable backend processes (*i.e.* metallization and interconnection) adopted from standard homojunction solar cell fabrication. While record cells of the past years made use of the interdigitated back-contact concept [1], mass production still favors classical H-pattern layouts with contacts at the front and rear side. Due to simplicity, screen printing of silver-containing low-temperature (LT) pastes for mass production has been the focus of research in past years [6, 7]. It has been shown that the weak adhesion of such metallization pastes (esp. busbars) to the wafer, makes the cell interconnection process by soldering very challenging [8–10]. Additionally, insufficient wetting of the LT metallization with liquid solder and little experience using Bi-based solder alloys regarding long-term stability impede the implementation of low-temperature soldering for SHJ cells. Consequently, alternatives such as interconnection with electrically conductive adhesives (ECAs) [11] and the Smart Wire Connection Technology (SWCT) [12, 13] have been explored.

Nevertheless, interconnection by soldering remains the simplest, most cost efficient and straightforward implementation into existing industrial fabrication lines. Due to continuous improvements in the formulation of the LT metallization pastes monitored within several projects at Fraunhofer ISE, contacting of the LT metallization with lead-based solders has become increasingly successful. In this work, peak temperatures of about 240 °C for very short times ($t < 3$ s) have been shown to be non-detrimental and create solder joints with sufficient adhesion (approaching 1 N/mm). Infrared soldering at ~240 °C enables the use of industrially

established equipment and to forgo alternative interconnection processes. The formation of well adherent void-free solder joints allows string handling, module integration and a detailed analysis of the solder joints, as shown in this study.

2 EXPERIMENTAL

2.1 Heterojunction solar cells

To study the interconnection process on SHJ solar cells by soldering, we use bifacial monocrystalline SHJ cells (156.75 × 156.75 mm²) of our project partner Meyer Burger (Germany) GmbH. The cells are pre-processed on *n*-type Cz-Si 6" wafers with *a*-Si:H(*i*)/*a*-Si:H(*n*+)/TCO on the front side and *a*-Si:H(*i*)/*a*-Si:H(*p*+)/TCO on the rear side. Metallization is screen printed in a five-busbar design on front and rear using various commercially available LT metallization pastes. After curing (10 min, 200 °C, convection furnace), the cells are interconnected on an industrial stringer at Fraunhofer ISE. Within this paper, the cured metallization is referred to as pastes for simplicity, although solvents and binders are evaporated during curing.

2.2 Infrared soldering

Soldering is done on an industrial stringer TT1800 of teamtechnik GmbH with an infrared (IR) soldering unit. We use conventional Sn60Pb40 solder coated copper ribbons (0.90 × 0.22 mm²) and no-clean flux. A typical soldering profile is sketched in Figure 1, in which the *y*-axis depicts the set-temperatures of the heating plates (green) and the IR lamps (red). The cycle time in this example is set to 2 s, which ends up in 1600 solar cells per hour passing through the stringer. Within the main heating zone, the IR radiation of two lamps heats the solder above its liquidus temperature $T_{liq} \approx 183$ °C to form an electrical and mechanical contact to the busbar. For this, two IR pulses each of 1.35 s duration at ~200 °C and ~240 °C set-temperature are used. After soldering, the quality of the solder joints on the both-side interconnected SHJ cells is analyzed mechanically and electrically, as described in the following.

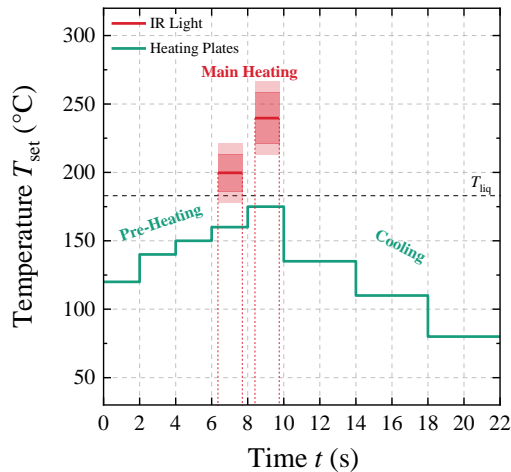


Figure 1: Schematic of the set-temperatures during infrared soldering of SHJ solar cells with an industrial stringer of teamtechnik GmbH using Sn60Pb40 solder.

2.3 Characterization

The mechanical strength of the solder joints is characterized using a Zwick Roell peel tester. The tests are done according to DIN EN 50461 with constant speed of 50 mm/min under an angle of 90°.

After the peel test, the fracture pattern is characterized with scanning electron microscopy (SEM) using an Auriga 80 microscope of Carl Zeiss Microscopy and energy diffractive X-ray (EDX) spectroscopy. Top view images are used to identify the failure mechanism of the interconnection.

In order to inspect the cross section of the solder joints, parts of the soldered SHJ cells are cut by a precision saw, embedded into a graphite-containing epoxy, ground and polished. The microstructure and quality of the solder joints is analyzed using SEM and EDX.

Additionally, 3D scans using X-ray micro-computed tomography (μ CT) reveal the inner structure and the microstructural quality of the solder bonds. This imaging technique enables to take 2D X-ray transmission images (projections) of a rotating object to reconstruct a 3D density model.

To analyze the effect of IR soldering at cell level, we conducted a coupled determination of the dark saturation current j_0 and the series resistance R_s (C-DCR) [14]. This spatially resolved measurement allows a local analysis of the electrical parameters R_s and j_0 of the solar cell based on luminescence imaging. We took several photoluminescence images at 1 sun and 0.1 sun and used the one-diode-model to determine j_0 as an approximation for a SHJ solar cell.

2.4 Module production

We built several 3-cell-modules for further temperature studies at module level with thermal cycling. The soldered SHJ cells are laminated at 145 °C for 10 min using a front glass ($200 \times 500 \times 3 \text{ mm}^3$), a thermoplastic polyolefin encapsulant and a white PET/Al/PET back sheet. To test the long term stability, a temperature cycling test (TC, $-40 \text{ }^\circ\text{C}/+85 \text{ }^\circ\text{C}$) according to IEC 61215 is performed. Prior and after the TC test, we take electroluminescence (EL) images and measure

the I-V parameters of the modules. Additionally, a full-size 60-cell-module with the same module materials, except for the glass where we used a glass with anti-reflective coating is built out of IR soldered SHJ cells and characterized electrically.

3 RESULTS

3.1 Mechanics and microstructure after IR soldering

In recent months, there has been progress in LT paste development and several companies released updated products. We test four of them regarding solderability and adhesion. The results of the 90° peel test after IR soldering at about 240 °C peak temperature with Sn60Pb40 coated ribbons are given in Figure 2. As reference, the best metallization paste of our work in 2017 (soldered manually with Sn60Pb40) [9] is also shown. Each data points includes 5 to 15 peel tests whereas the whole path along the busbar is considered (continuous busbars). Solder joints on the evaluated LT pastes show improved adhesion after IR soldering approaching 1 N/mm. The cells with paste 1 to 4a are soldered with a soldering time of $t_s \approx 3.0 \text{ s}$. For paste 4b, we reduced t_s to 1.35 s, which relates to an industrial throughput of 1600 solar cells per hour. With this adapted IR soldering process, an average peel force of $(0.91 \pm 0.20) \text{ N/mm}$ could be achieved, which is high enough for string handling and module integration.

In [9] it was shown that the adhesion is dominated by the microstructure of the LT paste. It was assumed that a finer grain structure assists infiltration of liquid solder and therefore supports ablation of the paste from the wafer surface. A coarser grain structure was correlated to a cohesive fracture after the peel test and therefore higher peel forces.

We also suspect the improvement of the adhesion shown in Figure 2 to be dominated by the paste composition itself. Therefore, we investigate the fracture pattern with SEM to identify the failure mechanism.

Figure 3 shows top view SEM images (InLens detector) of the fracture after the 90° peel test after IR soldering of paste 4a in (a) and (c) and of paste 2 in (b)

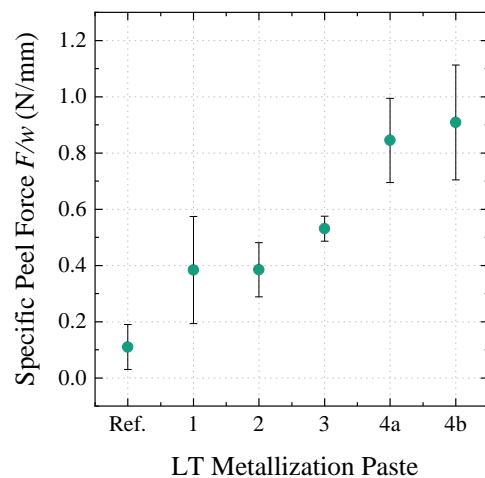


Figure 2: Peel force F normalized to ribbon width w of different metallization pastes after IR soldering with Sn60Pb40 solder alloy. The reference is taken from [9] and was soldered manually.

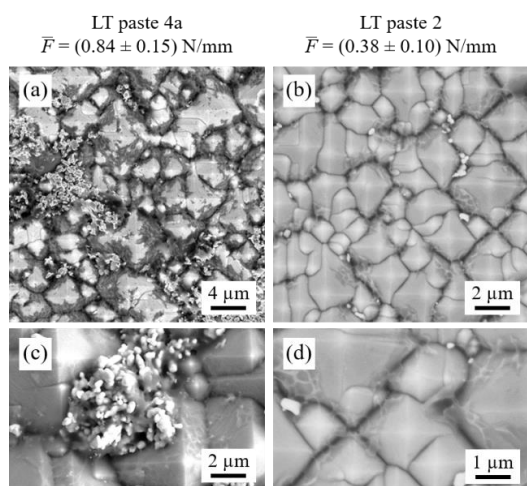


Figure 3: Top view SEM images of a fracture pattern after the peel test. (a), (c) Remnants of metallization paste 4a (0.84 N/mm) on the SHJ wafer surface. (b), (d) Adhesive failure to the Si wafer for paste 2 (0.38 N/mm).

and (d). Although most of the pyramids are visible, we find remnants of paste 4a, indicating a different failure mechanism than published before [8, 9]. For pastes with lower adhesion (*cf.* paste 2), the failure occurs adhesively between wafer surface and LT paste. With higher peel forces, more components of the pastes remain on the cell, leading to a more cohesive failure within the paste.

This finding correlates well with the microstructure of the solder joints, investigated in cross section images. Figure 4 shows the cross section of Sn60Pb40 solder joints on a bifacial SHJ solar cell with LT paste 4a. The optical microscopy image in (a) demonstrates the result of the both-sided interconnection process. The solder establishes an electrical and mechanical contact between the two Cu ribbons and the front and the rear busbar of the cell. An enlargement of the solder joint can be seen

in (b), where the solder/LT paste interface is shown. Wetting of the LT paste with liquid solder is sufficient to build a void-free solder joint for the used soldering parameters (~240 °C, 3 s). During soldering, the liquid solder seems to interact with the top layer of the LT paste. An EDX mapping in (c) and a close-up SEM image in (d) show the phase formation of Ag₃Sn. On the one hand, Sn of the solder diffuses into the LT paste (about 2 μm deep), on the other hand, some Ag particles of the LT paste top layer seem to penetrate into the liquid solder (about 1-2 μm deep) and partially dissolve. This defined Ag₃Sn phase formation (dashed white line in (c)) indicates a proper metallurgical bond [15].

Additionally, the larger grains of paste 4a seem to impede further penetration of solder into the busbar, as it was detected for the reference paste in [9].

A void-free interconnection could also be proven by X-ray micro-computed tomography (μCT) where we scan the interconnection area of an SHJ cell. On the right of Figure 5, the μCT image in 3D after reconstruction can be seen. From the center image (1), both ribbons (front and rear interconnection) can be seen to be perfectly aligned. Cutouts (2) and (3) of this measurement focus on the cell facing solder joints, which both show a homogeneous distribution of the solder, free of voids on front and rear.

This is an ideal condition for a mechanically stable and highly conductive solder joint and allows for string handling and module integration. Our characterization regarding adhesion and microstructure shows that IR soldering of up to ~240 °C (set-temperature) for 3 s is feasible to realize the interconnection of SHJ solar cells.

3.2 Electrical properties at device level after IR soldering

To address the impact of temperature during soldering on the electrical properties of the SHJ cells, we did C-DCR measurements to reveal possible local cell damages. Figure 6 shows the EL image and the C-DCR result of an interconnected SHJ cell, soldered at a set-temperature of 240 °C for 3 s (“IR standard”) in the top

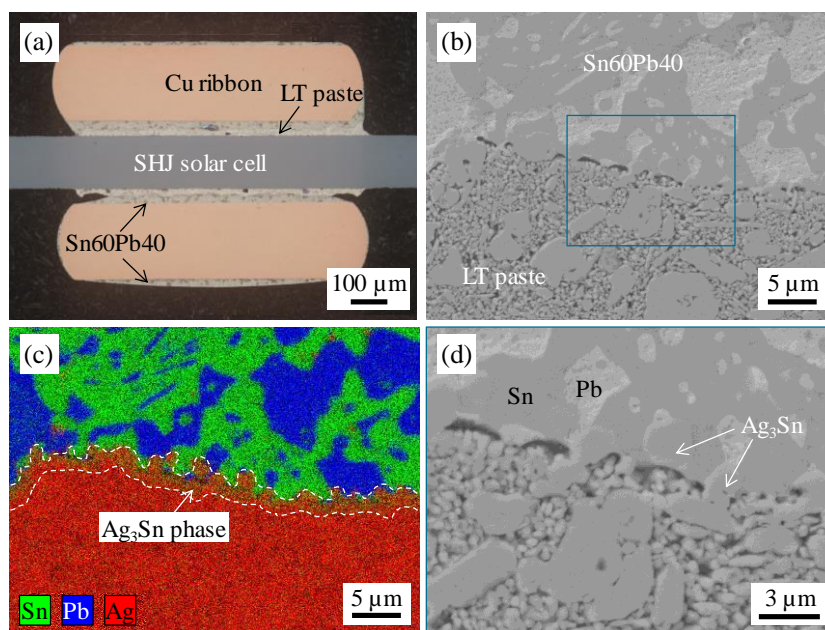


Figure 4: Cross section images of solder joints on bifacial SHJ solar cell with LT paste 4a. (a) Optical microscopy image. (b) SEM image of solder joint on the cell front side. (c) EDX mapping of (b). (d) Zoom into part of SEM image in (b).

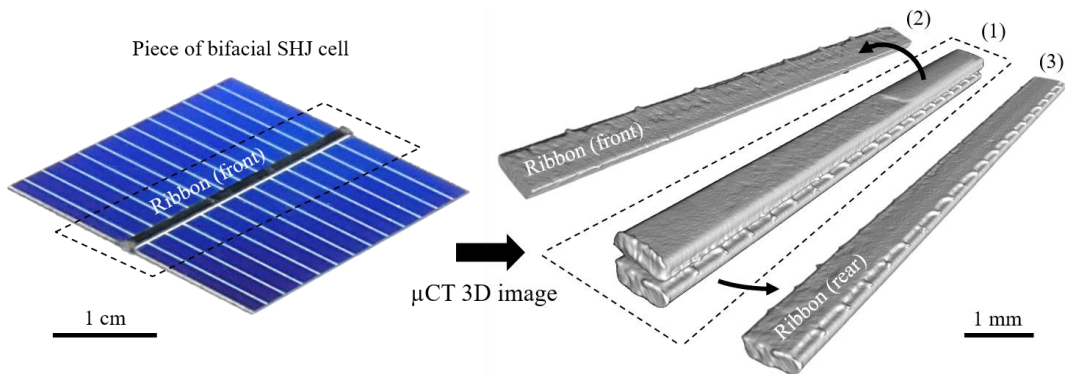


Figure 5: Photo of soldered SHJ solar cell piece (left). 3D X-ray micro-computed tomography (μ CT) image of SHJ solar cell after interconnection (right).

row. We could not detect any electrical cell damage for the used soldering profile. The bottom row shows the resulting images of a SHJ cell soldered at “hot” conditions, *i.e.* $\sim 310^\circ\text{C}$ set-temperature for 3 s. Here, degradation is clearly visible, especially in the regions between the busbars/ribbons. This can be attributed to an inhomogeneous temperature distribution in the IR field during soldering leading to local hot spots. The IR light is reflected by the metal parts of the setup (ribbons, downholder unit). Areas with less counts in the EL image correlate with a local increase of the series resistance R_s and the dark saturation current j_0 . This is mainly due to a local damage of the passivation layer (*e.g.* hydrogen effusion) which leads to a reduction of the open circuit voltage V_{oc} . The local series resistance increases which may be caused by a structural change of the a-Si and/or TCO layer influencing the electrical properties (charge carrier mobility μ and charge carrier density N) [16, 17]. Additionally, the interface between a-Si and TCO may suffer from high temperatures due to a reduced charge carrier transport, leading to an increase in R_s .

Nevertheless, $T_{set} \approx 310^\circ\text{C}$ as set-temperature for 3 s is far too hot to solder silicon solar cells to begin with.

The required soldering temperature is provided by the liquidus temperature T_{liq} of the used solder alloy. With the standard Sn60Pb40 alloy ($T_{liq} \approx 183^\circ\text{C}$), a peak temperature of $\sim 240^\circ\text{C}$ is sufficient to create a void-free solder joint, as experimentally shown in section 3.1.

Following these encouraging findings, the performance of IR soldered SHJ solar cells is investigated at module level in the next section.

3.3 Module integration

To build small format modules, we use industrial SHJ solar cells of Meyer Burger (Germany) GmbH with LT paste 4a. We again use our industrial stringer to solder the cells with IR light ($\sim 240^\circ\text{C}$, 3 s) using Sn60Pb40 coated Cu ribbons. 3-cell-modules are build and electrically characterized before and after the TC 200 test.

Figure 7 shows the I-V data of six 3-cell-modules after 200 temperature cycles. We normalize the values to the initial I-V parameters, respectively. Whereas I_{sc} and V_{oc} stay constant within scatter of the data, we measure a small fill factor (FF) decrease and power (P_{mpp}) loss of $< 1.0\%$. The analysis shows no critical decrease of the

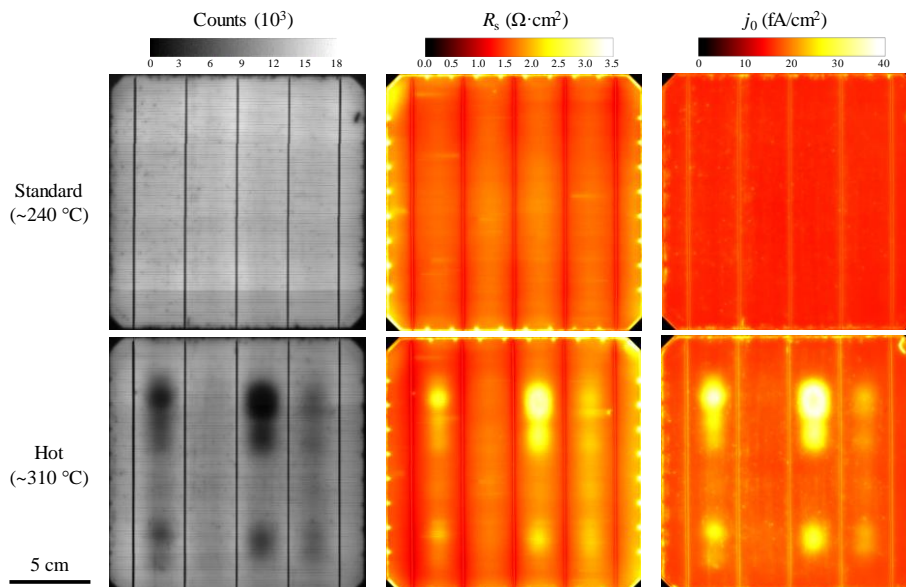


Figure 6: EL image (left column), series resistance (middle) and dark saturation current j_0 (right) of interconnected SHJ solar cells, IR soldered with Sn60Pb40 solder at standard ($\sim 240^\circ\text{C}$, 3 s) and hot ($\sim 310^\circ\text{C}$, 3 s) conditions.

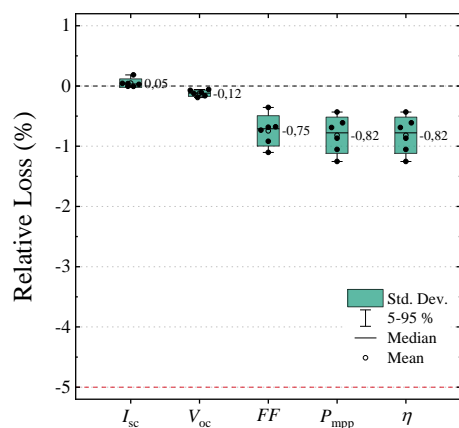


Figure 7: Relative degradation of the I-V parameters after TC 200 of six IR soldered 3-cell-modules with SHJ solar cells. The values are normalized to their corresponding initial value before TC.

relevant parameters (relative measurement uncertainties: I_{sc} : 1.5 %, V_{oc} : 0.6 %, FF : 1.4 %, P_{mpp} : 1.8 %, η : 1.9 %) and all modules pass the IEC criterion of a degradation smaller than 5.0 % within TC 200.

These promising mechanical and electrical results open the possibility of module integration into a 60-cell-module. We used industrially processed SHJ solar cells (full-size, n -type, bifacial, five busbar, average $P_{mpp} = 5.47$ W) and the same IR soldering parameters and similar module materials as for the 3-cell-modules. Figure 8 shows the corresponding EL image. A module power of 324 W could be demonstrated (monofacial measurement). The cell-to-module (CTM) power ratio for the realized module was calculated to be 98.8 %, which is in the range of typical industrial values [18, 19]. For an additional power improvement for a soldered SHJ module, one could use ribbons with a light reflective structure, half cells or even multi-wire SHJ interconnection.

4 SUMMARY

We analyzed the possibility of SHJ cell interconnection with standard soldering processes used for PERC solar cells. The process window for soldering SHJ cells is limited to lower peak temperatures compared to PERC cells. Process parameters as pre-heating, peak temperature and soldering time, as well as the used material combinations (metallization, TCO, solder alloy, ribbon) have to be chosen carefully and may influence the mechanical and electrical quality of the solder joint and therefore the performance of the module. Our experiments show that, in contrast to the reported temperature sensitivity for small-scale cells with a limit of ~ 220 °C [3, 4], SHJ cells can be IR soldered under industrial conditions (set-temperature $T_{peak} \approx 240$ °C for $t_s < 3$ s). Mainly depending on the low-temperature metallization paste, the adhesion after soldering was improved approaching 1 N/mm using Sn60Pb40 solder alloys. The formation of a defined Ag_3Sn phase at the solder/paste interface indicates a proper solder joint. We detect neither mechanical nor electrical cell damage after soldering and showed a TC stability of 3-cell-modules with an average power degradation < 1 %. A CTM power ratio of 98.8 % demonstrates a successful implementation

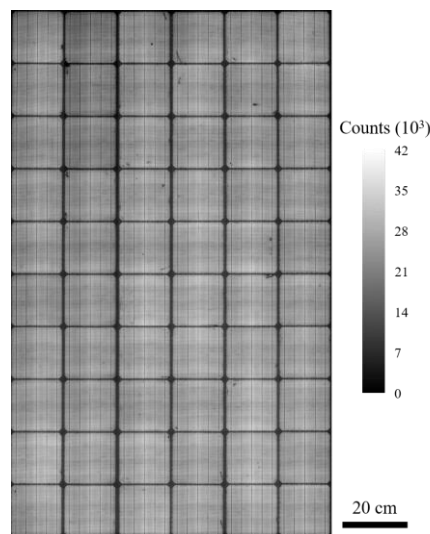


Figure 8: EL image of a SHJ 60-cell-module fabricated with IR soldering (~ 240 °C, 3 s) using Sn60Pb40 coated ribbons.

into a 60-cell-module fabricated with IR soldering and Sn60Pb40 solder alloy. This opens the opportunity for further power improvements using standard equipment known from PERC lines using half cells and ribbons with light reflecting structures or half cells in combination with *e.g.* multi-wire interconnection.

5 ACKNOWLEDGEMENT

This project was funded by the German Ministry for Economic Affairs and Energy within the research project “HJT 4.0” under contract number 0324172.

A.D.R. would like to thank all coworkers at Fraunhofer ISE for discussions and measurements.

6 REFERENCES

- [1] K. Yoshikawa *et al.*, “Silicon heterojunction solar cell with interdigitated back contacts for a photoconversion efficiency over 26%,” *Nat. Energy*, vol. 2, no. 5, p. 17032, 2017.
- [2] D. Adachi, J. L. Hernández, and K. Yamamoto, “Impact of carrier recombination on fill factor for large area heterojunction crystalline silicon solar cell with 25.1% efficiency,” *Appl. Phys. Lett.*, vol. 107, no. 23, p. 233506, 2015.
- [3] B. A. Korevaar, J. A. Fronheiser, X. Zhang, L. M. Fedor, and T. R. Tolliver, “Influence of annealing on performance for hetero-junction a-Si/c-Si devices,” in *Proceedings of the 23rd European Photovoltaic Solar Energy Conference and Exhibition*, Valencia, Spain, 2008, pp. 1859–1862.
- [4] S. De Wolf and M. Kondo, “Nature of doped a-Si:H/c-Si interface recombination,” *Journal of Applied Physics*, vol. 105, no. 10, 103707, 2009.
- [5] J. Haschke *et al.*, “Annealing of Silicon Heterojunction Solar Cells: Interplay of Solar Cell and Indium Tin Oxide Properties,” *IEEE J. Photovoltaics*, pp. 1–6, 2019.

- [6] D. Erath *et al.*, “Comparison of innovative metallization approaches for silicon heterojunction solar cells,” *Energy Procedia*, no. 124, pp. 869–874, 2017.
- [7] J. Schube, M. Weil, T. Fellmeth, R. Keding, and S. W. Glunz, “Intense Pulsed Light Meets the Metallization of Silicon Heterojunction Solar Cells,” in *46th IEEE Photovoltaic Specialists Conference (PVSC)*, Chicago, Illinois, 2019.
- [8] P. Gierth *et al.*, “Comparison of NiV and Polymer Paste Metallization as Low Temperature Interconnection of High Efficiency Heterojunction Solar Cells,” in *Proceedings of the 28th European Photovoltaic Solar Energy Conference and Exhibition*, Paris, France, 2013, pp. 464–467.
- [9] A. De Rose, D. Erath, T. Geipel, A. Kraft, and U. Eitner, “Low-temperature soldering for the interconnection of silicon heterojunction solar cells,” in *Proceedings of the 33rd European Photovoltaic Solar Energy Conference and Exhibition (EU PVSEC)*, Amsterdam, 2017, pp. 710–714.
- [10] A. De Rose, T. Geipel, D. Erath, A. Kraft, and U. Eitner, “Challenges for the interconnection of crystalline silicon heterojunction solar cells,” *Photovoltaics International*, vol. 40, pp. 78–86, 2018.
- [11] T. Geipel *et al.*, “Industrialization of the ribbon interconnection of silicon heterojunction solar cells with electrically conductive adhesives,” *at this conference*, ttp. 2019.
- [12] A. Faes *et al.*, “Smartwire solar cell interconnection technology,” in *Proceedings of the 29th European Photovoltaic Solar Energy Conference and Exhibition*, Amsterdam, Netherlands, 2014, pp. 2555–2561.
- [13] P. Papet *et al.*, “New Cell Metallization Patterns for Heterojunction Solar Cells Interconnected by the Smart Wire Connection Technology,” *Proceedings of the Fifth Workshop on Metallization for Crystalline Silicon Solar Cells*, vol. 67, pp. 203–209, 2015.
- [14] M. Glatthaar *et al.*, “Spatially resolved determination of dark saturation current and series resistance of silicon solar cells,” *physica status solidi (RRL) – Rapid Research Letters*, vol. 4, no. 1-2, pp. 13–15, 2009.
- [15] T. Geipel, M. Moeller, A. Kraft, and U. Eitner, “A comprehensive study of intermetallic compounds in solar cell interconnections and their growth kinetics,” *Energy Procedia*, vol. 98, pp. 86–97, 2016.
- [16] L. Tutsch *et al.*, “Implementing transparent conducting oxides by DC sputtering on ultrathin SiO_x / poly-Si passivating contacts,” *Sol Energ Mat Sol C*, vol. 200, pp. 1–5, 2019.
- [17] N. Juneja *et al.*, “Effect of Hydrogen Addition on Bulk Properties of Sputtered Indium Tin Oxide Thin Films,” in *9th International Conference on Crystalline Silicon Photovoltaics (SiliconPV)*, Leuven, Belgium, 2019.
- [18] ITRPV, “International Technology Roadmap for Photovoltaic (ITRPV): 10th edition, 2018 Results,” 2019. Accessed on: Apr. 23 2019.
- [19] I. Hädrich, “Unified methodology for determining CTM ratios: Systematic prediction of module power,” in *Proceedings of the 4th International Conference on Crystalline Silicon Photovoltaics*, 's-Hertogenbosch, Netherlands, 2014.